

Lock-in Detection based Dynamic Widefield Magnetometry using Quantum Defects in Diamond

Madhur Parashar,^{1,2,*} Dasika Shishir,³ Anuj Bathla,⁴ Alok Gokhale,³ Sharba Bandyopadhyay,¹ and Kasturi Saha^{3,†}

¹*Information Processing Laboratory, Department of Electronics and Electrical Communication Engineering, Indian Institute of Technology Kharagpur, Kharagpur, West Bengal, India - 721302*

²*School of Medical Science and Technology, Indian Institute of Technology Kharagpur, Kharagpur, West Bengal, India - 721301*

³*Department of Electrical Engineering, Indian Institute of Technology Bombay, Mumbai, Maharashtra, India-400076*

⁴*Centre for Research in Nanotechnology and Science, Indian Institute of Technology Bombay, Mumbai, Maharashtra, India-400076*

Wide field-of-view magnetic field microscopy has been realised by probing shifts in optically detected magnetic resonance (ODMR) spectrum of nitrogen vacancy (NV) defect centers in diamond. However, these widefield diamond NV magnetometers require few to several minutes of acquisition to get a single magnetic field image, rendering the technique as temporally static in its current form. This limitation prevents application of diamond NV magnetometers to novel imaging of dynamically varying microscale magnetic field processes. Here, we show that the magnetic field imaging frame rate can be significantly enhanced by performing lock-in detection of NV photo-luminescence (PL), simultaneously over multiple pixels of a lock-in camera. A detailed protocol for synchronization of frequency modulated PL of NV centers with fast camera frame demodulation, at few kilohertz frequencies, has been experimentally demonstrated. This modified diamond NV imaging allows up to ten thousand pixels to simultaneously track an applied magnetic field waveform of sub-second temporal variation at imaging frame rates of 50 – 200 Hz. Our work demonstrates that widefield per-pixel lock-in detection, in combination with frequency modulated NV ODMR, enables millisecond scale dynamic magnetic field microscopy.

I. INTRODUCTION

The past decade has seen a revolution in high-resolution diffraction-limited microscale and wide field-of-view magnetometry based on optically detected magnetic resonance (ODMR) imaging of Nitrogen Vacancy (NV) defect centers in diamond [1–6]. These room-temperature ultra-sensitive diamond NV magnetometers [7–10] have enabled a new class of magnetic field microscopy, for example - probing magnetic particles in living cells [3, 11], imaging fluid-like current flow in graphene [6, 12], microscopy of novel quantum materials [13] and rapidly evolving other applications [14–17]. In diamond NV-based widefield magnetic field imaging (WM), red photo-luminescence (PL) emitted from a microscale volume of NV centers is collected and imaged on to a conventional scientific CMOS or CCD camera. Microwave resonant frequencies applied to NV centers create changes in NV fluorescence and the precise estimation or tracking of these resonant MW frequencies yields a 2D microscale magnetic field map. The changes in magnetic field experienced by small microscopic volumes of NVs in the diamond crystal get mapped to corresponding pixels on the camera pixel array. However, magnetic field images acquired by this method have remained temporally static in nature, demanding few to several minutes of acquisition time for each image frame [4, 6, 11]. Inherently low NV ensemble resonance contrast and division of informative NV light onto thousands to

millions of pixels, significantly decrease per-pixel signal-to-noise ratio (SNR) and consequently the magnetic field sensitivity. NV WM imaging frame rate for DC to low-frequency magnetometry is fundamentally limited by the NV optical re-polarization rate i.e. ~ 1 MHz. However, practical SNR bounds have limited imaging frame rates to primarily static magnetic field maps. Development of high-spatially-resolved and high-frame-rate imaging capabilities will enable new applications of NV centers to investigate processes like vortex dynamics in superconductors [18], estimating fluctuating magnetic fields from quantum materials [13], magnetic nano-particle motion in living cells [11, 19] and imaging mammalian action potential associated magnetic fields [20–23].

Detection of weak signals embedded in noise hinges on smart techniques such as the lockin-amplification method, wherein a near-DC or slowly varying signal, mainly submerged in $1/f$ noise, can be periodically modulated and filtered from a narrow band while the noise spanning a large bandwidth can be eliminated leading to significant improvement in signal-to-noise ratio. Pico-Newton scale resolution in atomic force microscopy [24] and high sensitivity magnetometry in SQUIDS and atomic magnetometers [25] are testament to this detection methodology. With advent of lock-in cameras [26], parallel per-pixel lock-in detection of optical light can be performed over many pixels. In contrast to conventional cameras, the lock-in cameras require synchronized external triggers to perform light integration over specific time windows for each pixel. Intensity measured during these externally timed windows can be used to subtract DC components and estimate the frequency content of the optical signal. With these high frame rate

* madhurparashar@iitkgp.ac.in

† kasturis@ee.iitb.ac.in

lock-in cameras, new improvements have been observed in techniques where light can be frequency or phase modulated, *e.g.*, deep tissue optical coherence tomography (OCT) [27] and ultrasound-modulated OCT [28] and other avenues [29, 30]. NV emitted light can be frequency modulated by microwave control of NV resonance [31]. Frequency modulated optically detected magnetic resonance (fm-ODMR) schemes for NVs have been used for real-time single point (SP) bulk magnetometry [20, 22, 32–34], where total emitted NV light is collected onto a single photodetector and also for boosting DC-magnetic field sensitivity. A prior work on camera review [35] has also suggested potential application of high-frame rate lock-in camera to perform real-time NV WM imaging.

In this work, we demonstrate a novel per-pixel lock-in detection that enables dynamic millisecond scale magnetic field imaging in wide-field using NV centers in diamond. The paper describes a procedure for synchronizing camera frames of a commercial lock-in camera (Heliotis Helicam C3 [36]) with NV microwave modulation to obtain fm-ODMR across thousands of pixels. Post calibration of noise statistics and magnetic field sensitivity across different pixels, we measured a mean $22.18 \mu\text{T}/\sqrt{\text{Hz}}$ sensitivity per pixel. We discuss how imaging frame rates and per-pixel SNR are coupled to the NV modulation frequency and the number of signal averaging cycles. Finally, we show a novel demonstration of NV-based WM imaging of a square wave magnetic field varying at a few seconds timescale, imaged at millisecond frame rates. Multiple pixels can track the test magnetic field applied uniformly over all pixels. We show WM imaging of a 1.28 Hz magnetic field variation at 38.6 Hz imaging frame rate. To demonstrate scalability of imaging frame rates, tracking of ~ 7 Hz magnetic field variation at ~ 200 Hz imaging frame rate at reduced SNR is also shown. Our experiments demonstrate that frequency-locked widefield imaging of NV emitted light may enable dynamic widefield magnetic field imaging at rates ranging from 10 – 200 Hz. The scope of the work demonstrated in this paper is not limited to just imaging diamond crystals, but can also be extended to perform improved temporal imaging of nanodiamonds in cellular environments [37–39].

II. EXPERIMENTAL METHODS

A. Magnetic resonance in nitrogen vacancy defects in diamond

Negatively charged nitrogen-vacancy defect centers in diamond are point localized Nitrogen substitution of Carbon in the diamond lattice with an adjacent vacancy and an overall negative charge. Due to their unique electronic properties these vacancies [9], are sensitive to external environment changes like, magnetic field, electric field, strain and temperature. The ground state exists as a

spin-triplet whose sub-levels exist as a singlet $m_s = 0$ and a double degenerate $m_s = +1$ and $m_s = -1$, in absence of magnetic field. The degeneracy of $m_s = +1$ and $m_s = -1$ is lifted by Zeeman splitting in the presence of an external magnetic field. Transitions to the excited state are spin conserved, however, the relaxation from excited triplet state take two paths – a radiative spin conserving path and a non-radiative decay via intersystem crossing (ISCs). The radiative decay produces broadband red photo-luminescence with the zero-phonon line at 637 nm. The non-radiative ISCs are highly spin-selective towards the $m_s = 0$ spin sublevel. Therefore, continuous optical excitation leads to electron spin polarization. Neglecting the hyperfine interaction between the nuclear spin of the Nitrogen atom the NV’s electronic spin, the ground state NV Hamiltonian is given by

$$H = hDS_z^2 + hE(S_x^2 - S_y^2) + g\mu_B B \cdot S, \quad (1)$$

where, h is the Planck’s constant, D is the zero-field splitting, μ_B is the Bohr magneton, g is the gyromagnetic ratio, E is the applied electric field and the last term corresponds to the Zeeman term, with B , the externally applied magnetic field. S_x, S_y, S_z correspond to the Pauli matrices for a spin-1 system. In the weak-field regime where $B_\perp \ll B_\parallel$, the electron spin resonance frequencies are given by

$$\nu_\pm(B_{NV}) = D \pm \sqrt{\left(\frac{g\mu_B}{h}B_{NV}\right)^2 + E^2} \quad (2)$$

where, B_{NV} is the component of the applied field parallel to the NV axis. For cases where applied bias field is high enough to neglect the E term, the electron spin resonance frequencies vary linearly with the applied magnetic field. Such a regime is ideal for sensitive magnetometry with diamond NV centers.

B. Experimental setup

Fig. 1a is an illustration of the experimental setup used to perform diamond NV magnetometry. A non-resonant green light excitation at 532 nm (Sprout Laser) is used to illuminate NV centers via a 60 \times objective (Olympus, UPLNFLN series). Optical power impinging the objective back aperture is $\sim 1.5W$. We use a non-electron irradiated, CVD (chemical vapor deposition) grown diamond with Nitrogen concentration $[N] = 50$ ppm (purchased from Diamond Elements Inc. Surat, India) that has naturally formed NV centers distributed in bulk across the entire thickness of the sample. The emitted light from NV centers is collected via the same objective, filtered to select red light (above 567 nm) and reject green excitation light (532 nm notch stop filter (SEM-ROCK NF03-532E-25)). The collected light is focused onto a widefield lock-in camera (Heliotis Helicam C3) or a photodiode (Thorlabs DET 100A) to perform either widefield magnetometry or single-point magnetometry.

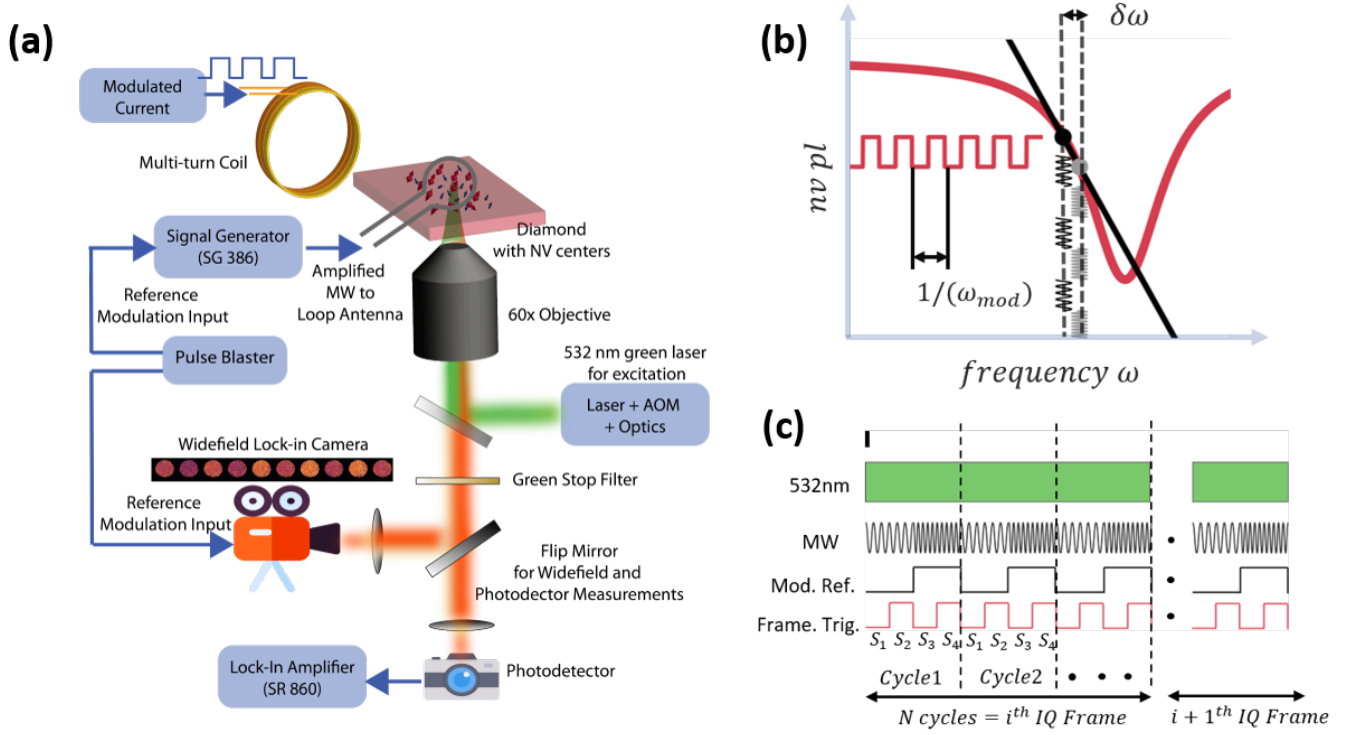


FIG. 1. Schematic of the experimental setup and protocol for data acquisition. (A) Schematic describing the experimental setup for single photodiode diamond NV magnetometry (SP) or widefield per pixel lock-in diamond nitrogen-vacancy magnetometry (WM) (B) Illustration explaining generation of frequency modulated NV emitted red light by applying frequency shift key type microwave resonant frequencies. The applied microwave resonant frequencies shuttle between ω and $\omega - \omega_{dev}$ in sync with square wave waveform of frequency ω_{mod} . When the microwave frequencies are resonant, the emitted NV red light is frequency modulated at ω_{mod} (C) Pulse protocol to control and synchronize the demodulation of internal camera frames with modulation frequency of optical signal to obtain lock-in in-phase (I) and quadrature (Q) images. A green laser illumination at 532nm is always on and frequency shift key microwave (MW) waveform with modulation ω_{mod} are applied. Lock-in camera external trigger pulses, controlling internal frame acquisition timings, are provided at $2\omega_{mod}$, synced with MW modulation, where they define 4 quarters for light integration $S_1 S_2 S_3 S_4$. These four quarters of light integration allow in-phase ($S_1 - S_3$) and quadrature ($S_2 - S_4$) estimation of optical signal and are averaged over N cycles to give single pair of In-phase image and Quadrature Image (IQ Frame)

The diamond sample is mounted on a coplanar waveguide resonator [40], and associated microwave electronics are used to deliver microwave frequencies in the range $\sim 2.5 - 3.2$ GHz at power -5 dBm before amplification (~ 40 dB gain). The applied microwave frequencies follow frequency shift keying waveforms with square-wave envelopes. The camera imaging frames are synchronized with the microwave modulation with specific pulse sequences generated by a high-speed TTL pulse generator card (SpinCore PulseBlaster ESR-PRO 500 MHz). Further, a calibrated, test magnetic field is externally applied to demonstrate the temporal tracking performance of the magnetometer. Neodymium disk magnets are used for applying a bias magnetic field and have not been shown in the experimental schematic.

C. NV Frequency Modulation and Synchronization of Lock-in Camera

The generation of modulated NV light with frequency ω_{mod} in the fm-ODMR protocol is shown via the schematic shown in Fig. 1b. In a frequency shift keying waveform, two microwave frequencies ω and $\omega - \delta\omega$ are delivered via the MW resonator, where they shuttle between each other with the square wave waveform of frequency ω_{mod} . For each MW frequency, the NV fluorescence settles to a steady-state value, given by the NV's resonance curve at the applied MW frequency. To measure the amplitude of modulated NV PL, we perform lock-in detection of the collected light in SP or WM mode at reference frequency ω_{mod} . For the rest of the article, by referring to the 'modulation frequency' of NVs, we also mean the 'reference frequency' of the lock-in amplifier or the lock-in camera. We found magnetic field sensitivity of $11.6 \text{ nT}/\sqrt{\text{Hz}}$ in SP lock-in magnetometry,

which was measured with a photodetector and a lock-in amplifier (SR860). Real-time magnetic field tracking of a square wave magnetic field of amplitude 28.5 nT with SP magnetometry has been shown in Supplementary Figure S1.

To synchronize the applied MW waveform with the camera's internal frames, an external reference signal of $2\omega_{mod}$, carefully synced to MW modulation reference at ω_{mod} , is provided to the camera's external trigger input, see Fig. 1c. This TTL signal, of twice the modulation frequency, defines the four quarter periods of sensor light integration whose values are denoted by S_1, S_2, S_3, S_4 . The in-phase signal is $S_1 - S_3$ and the quadrature signal $S_2 - S_4$. Additionally, as shown in the schematic Fig. 1c, each cycle of demodulation is internally averaged N times to provide a single pair of 2D images containing in-phase (I) and quadrature (Q) values for each pixel. Therefore, to get a single 2D IQ image, the total time is $(1/2\omega_{mod}) * cyc$, which sets the imaging frame rate. Further, since the NV signal scales with ω_{mod} different imaging frame rates have different SNR as discussed later. The lock-in camera is limited to frame rates of 3.2 kHz and a maximum 250 kHz signal demodulation.

III. RESULTS

A. Optically detected magnetic resonance of multiple pixels

Optically detected resonance spectrum of an ensemble of NV centers corresponding to each pixel on the Helicam C3 Array is shown in Fig. 2(a). A 2D array of 100×100 pixels have been concatenated into a 1D vector of 10,000 pixels and their lock-in ODMR response across multiple microwave excitation frequencies has been color-coded. Three randomly selected pixel's individual ODMR traces have been shown in Fig. 2(b). For each pixel, the NV response curve can be described by Lorentzian

$$f(\omega) = A \left[1 - \frac{C}{1 + \left(\frac{\omega - \omega_0}{\Gamma} \right)^2} \right], \quad (3)$$

where $A, C, \Gamma, \omega, \omega_0$ denote baseline PL, contrast, the linewidth of resonance, MW frequency applied, and resonant MW frequency of the NV center respectively. The lock-in signal is proportional to the derivative of the NV ODMR response curve in Eq. (3). The derivative of the response curve with an added baseline term was used to fit the lock-in ODMR response, examples shown in Fig. 2(c) and (d). To highlight the importance of NV modulation frequency and frame averaging, two examples of ODMR traces (Fig. 2(C) and Fig. 2(d) acquired at different NV modulation frequencies (6.25 kHz and 8.33 kHz) and frame averaging cycles (122 cycles and 82 cycles respectively) are shown. The slope at the zero-crossing point of the fm-ODMR response curve along

with the noise floor are critical factors that determine the magnetic field sensitivity of each pixel. In agreement with previous studies [31], we observe reduced zero-crossing slope at higher modulation frequency due to reduced NV interaction time with the resonant microwave frequencies, oscillating between ω and $\omega - \omega_{dev}$. By comparing the jitter in response at non-resonant NV frequencies in Fig. 2C,D, we observe a reduction in the noise floor of pixels at less frame averaging cycles. These examples briefly illustrate a trade-off between NV response signal and noise floor at different parameters. Further, the imaging frame rate is dependent on the ratio between modulation frequency to averaging cycles (see Methods, HelicamC3 synchronization), and hence is coupled to the SNR of the NV ODMR response.

B. Per-pixel magnetic field sensitivity

As evident from the two example ODMR traces at different acquisition rates, the noise statistics and fm-ODMR signal of pixels can vary significantly with image acquisition parameters. Typically, the sensitivity of a sensor is defined by the ratio of uncertainty in the measurement to the maximum slope point *i.e.* the point of operation of the sensor where the smallest perturbation in the input creates maximal change in the output of the sensor. Specifically, for fm-ODMR the slope is maximum at the zero-crossing of the lock-in voltage, also corresponding to the resonant frequency of NV centers. Therefore, the magnetic field sensitivity is defined as

$$\eta = \frac{\sigma\sqrt{\tau}}{\left. \frac{dV_{lock}}{df} \right|_{V_{lock}=0, f=\omega_{res}}} \quad (4)$$

where σ is the standard deviation of measurement (voltage for lock-in amplifier or arb. units for camera) and τ is the measurement time of the signal. The denominator denotes slope at the resonant frequency ω_{res} .

First, $\sigma\sqrt{\tau}$ statistics were collected for both SP and WM experiments, with identical red light collection as would be collected during the fm-ODMR experiments, except no microwave frequency was applied. For SP experiments, we observed the typical sharp $1/f$ decrease in σ versus ω_{mod} spectrum (See Supplementary Fig. 2A), which explains the large gain in SNR when NV emitted light is modulated and measured at higher frequencies.

To acquire σ statistics for WM experiments, twenty image frames were acquired and the mean and standard deviation of each pixel's intensity were recorded (see example Supplementary Fig. 2B, C). The WM σ spectrum for most pixels remained mostly flat, as compared to SP σ spectrum, between modulation frequencies of 3 KHz to 100 KHz, with mean value of 7.69 units (out of 10-bit 1024 point scale) for all pixels in Fig. 3(a). Since the minimum possible camera modulation frequency is 2.2 kHz, most of the low-frequency noise is not visible

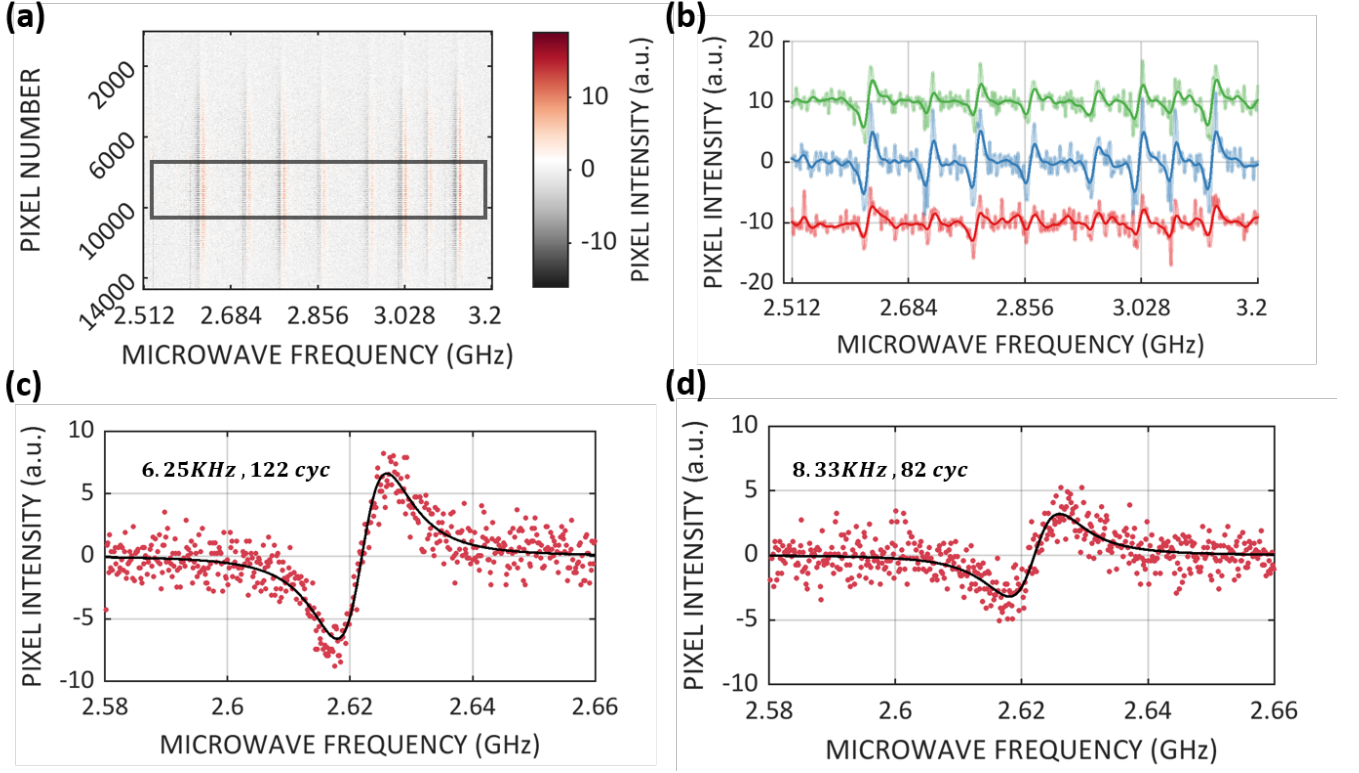


FIG. 2. Frequency modulated optically detected magnetic resonance spectrum (ODMR) of multiple pixels. (A) A 2D array of 100X100 pixels has been concatenated into a 1D array of pixels and their magnetic resonance response have been color coded. We observe 8 NV resonant frequencies across multiple pixels. A rectangular box represents that few randomly selected individual pixel ODMR responses have been shown in the next subplot (B) 3 example ODMR response traces have been shown for randomly selected pixels. The baseline of the pixels, centered at 0, has been shifted to represent them in the same plot (C) Example pixel ODMR response data recorded at 6.25 kHz modulation frequency and 122 frame averaging cycles. Each red dot represents data at single microwave frequency and black curve represent non-linear Lorentzian-derivative curve fit (D) Example pixel ODMR response data recorded at 8.33 kHz modulation frequency and 82 frame averaging cycles. Each red dot represents data at single microwave frequency and black curve represent non-linear Lorentzian-derivative curve fit. Reduced ODMR zero-crossing slope and reduced noise floor can be observed at faster modulation frequencies and lesser frame averaging cycles

in the WM noise spectrum. For SP experiments, the measurement time τ was set as per the settling time of the lock-in amplifier low pass filter with time constant τ_{lockin} , $\tau = 4 * \tau_{lockin}$, whereas for WM experiments we set $\tau = (1/\omega_{mod}) * n_{cyc}$, where n_{cyc} was the number of frame averaging cycles. To measure the zero-crossing slope, we selected a resonant frequency with a high peak-to-peak signal out of 8 resonant frequencies, and acquired an ODMR spectrum for the resonant frequency at high MW step size (100 kHz). We estimated the slope at zero-crossing for each pixel by non-linear curve fitting (see example pixel fits in Supplementary Fig.3C). Finally, we show the 2D sensitivity map (Fig.3a), depicting a spatial variation of pixel sensitivity, by evaluating Eq.(4) for each pixel. Pixels with high response fall within the center of the NV PL intensity profile and pixels with low or no response fall towards the outer periphery of the NV PL intensity profile. We observed a heterogeneous sensitivity profile, due to the variation

of MW power and optical power in the NV excitation volume. We measured SP sensitivity of $11.6 \text{ nT}/\sqrt{\text{Hz}}$, evaluated by Eq.4. The distribution of per-pixel sensitivity, see Fig.3(b), has been shown, and mean and median pixel sensitivity was found to be $22.18 \text{ } \mu\text{T}/\sqrt{\text{Hz}}$ and $17.34 \text{ } \mu\text{T}/\sqrt{\text{Hz}}$ respectively. Only pixels with sensitivity more than $55 \text{ } \mu\text{T}/\sqrt{\text{Hz}}$ have been considered to remove pixels with very weak ODMR signals near the edges of the NV emitted beam (see Supplementary Figure S3D for all-pixels included sensitivity map). Additionally, before the curve fitting for each pixel, a selection threshold was applied to select pixels with a minimum threshold level of fm-ODMR response (see Supplementary section 2) and only the responding pixels were further analyzed.

Sensitivity η scales as $1/\sqrt{N}$, where N is the number of NV spins [41]. To correlate our SP bulk sensitivity with per-pixel sensitivity, we note that $\eta \propto 1/\sqrt{N} \propto 1/\sqrt{(V)} \propto 1/\sqrt{l^3}$ where V, l is total volume and length of side of each pixel, assuming the total volume to be

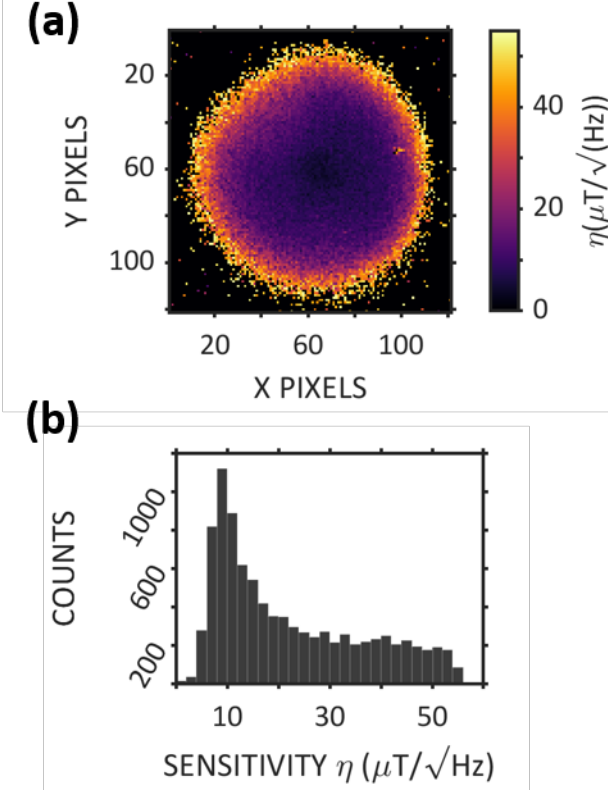


FIG. 3. Measurement Noise and Sensitivity per pixel (A) Measured 2D map of sensitivity of all responding pixels. Pixel numbering represents pixels on the lock-in camera array. Pixels with sensitivity better than $55\mu\text{T}/\sqrt{\text{Hz}}$ have been included. (B) Histogram of sensitivity of all responding pixels, with mean at $22.18\mu\text{T}/\sqrt{\text{Hz}}$

divided into equal-sized cubes. Therefore, for a circular responsive area of radius 50 pixels (with $55\mu\text{T}/\sqrt{\text{Hz}}$ sensitivity cutoff), the WM per-pixel sensitivity should decrease by a factor of 834.29 of the total SP sensitivity. The ratio of our mean per-pixel WM sensitivity to SP sensitivity is 1912.47. The difference in the two ratios can be accounted by the following two reasons. First, in mean per-pixel sensitivity, we consider the average of only responding pixels but some pixels with very low signal at the periphery have been left out from calculations and tracking experiments. However, these pixels also receive a fraction of NV emitted light and therefore, contribute to the SP sensitivity but not to the mean WM per-pixel sensitivity evaluated here. Second, in the relation $\eta \propto 1/\sqrt{l^3}$, we assume that the detector noise limits remain the same. However, we use different light detectors in SP and WM experiments, and therefore the noise variability $\sigma\sqrt{\tau}$ term differs in the two cases. Further, if we include all pixels for WM per-pixel mean sensitivity calculation, the actual and expected ratios of WM per-pixel sensitivity to SP Sensitivity differ by an order of magnitude as many pixels are excited with either too low optical or MW power and hence, $\eta \sim 1/\sqrt{N}$ propor-

tionality does not hold.

To further verify per-pixel sensitivity, we analyzed the magnetic field noise density of SP as reference and WM example pixel data. The amplitude spectral density (ASD) of magnetic field noise in SP-mode (Supplementary Fig. 4A) has been measured for four cases - electronic noise ($0.325\text{ nT}/\sqrt{\text{Hz}}$), microwave frequency on and at off NV resonance frequency ($5.3\text{ nT}/\sqrt{\text{Hz}}$), microwave frequency on and at NV resonance frequency ($2.1\text{ nT}/\sqrt{\text{Hz}}$) and microwave frequency off ($2.3\text{ nT}/\sqrt{\text{Hz}}$). As expected, we found the electronic noise floor, ASD mean between 0.9 Hz to 100 Hz, to be an order lower than the other measurements. The SP ASD noise floor values obtained from the four cases are also in close agreement with the measured SP sensitivity from the Eq. 4, with small differences arising from considering ASD noise floor over the frequency range of 0.9 Hz to 100 Hz only. With the SP as reference, we found similar ASD profile for an example pixel (Supplementary Fig.4B), where the noise floor was ($51.47\mu\text{T}/\sqrt{\text{Hz}}$), mean of ASD between 0.9 Hz to 10 Hz.

We next investigate the nature of the noise in the system for the case of SP and WM. Shot noise or Gaussian noise, dominates in our measurements, we look at variability (standard deviation) of the NV-ODMR optical signal in a microwave range containing a NV resonant frequency. In the shot noise regime, the variance of the lock-in signal will be dependent on the applied microwave frequency, as the NV-ODMR optical signal varies in amplitude near the resonant frequency. In Gaussian noise regime, inspite of the presence of NV-ODMR response in the given MW frequency range, the variance of the lock-in signal will not depend on applied MW frequencies, and is expected to fluctuate about a constant baseline. For SP case, with lock-in amplifier recordings at high low-pass time constant 30 ms (more averaging cycles), we observed dependence of standard deviation of the NV-ODMR signal on applied MW frequencies (Fig. 4 (A)), indicating shot noise dominance. Each measurement at a particular MW frequency, was averaged over 100ms interval and repeated 30 times to obtain noise statistics. Scatter plots of the variance versus the absolute mean of the optical signal, with data pooled from Fig. 4 (A), denote a linear trend (Fig.4(B)), confirming shot-noise dominated regime. However, in SP measurements at low low-pass time constant of 1ms (less signal averaging cycles), we did not observe dependence of the standard deviation of the signal on the applied MW frequencies (Fig.4(C)). Each measurement at a particular MW frequency, was averaged over 10ms interval and repeated 100 times to obtain noise statistics. For this measurement case, scatter plots of the variance versus the absolute mean of the optical signal do not show any increasing linear trend. While 1ms filter constant allows faster acquisition, less averaging cycles and decreased NV-ODMR SNR allow other sources of noise to dominate and yield a Gaussian noise dominated regime.

Similar to SP, we collected WM NV-ODMR noise

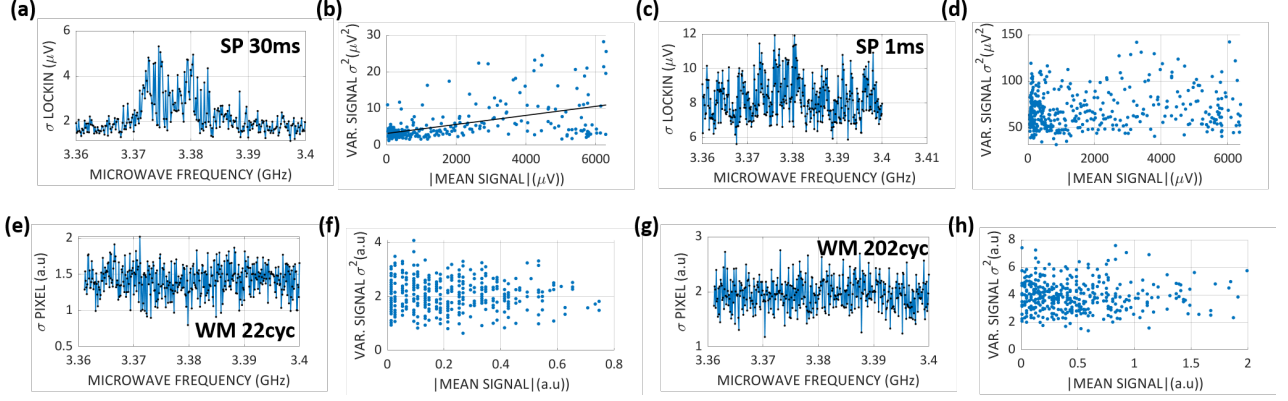


FIG. 4. Measurements depicting different noise statistics of the single point lock-in magnetometry (SP) and widefield magnetometry (WM). For these experiments, both SP and WM measurements were known to have a single resonance peak in the window 3.36 – 3.4 GHz. (A) Standard deviation σ of in-phase lock-in voltage (low-pass filter time constant at 30 ms) versus microwave resonance frequency applied. Black dots indicate evaluated σ at each MW data-point and the blue curve joins them. The σ shows dependence on the NV-ODMR signal for SP, time constant=30 ms case. (B) Scatter plot of variance ($(\mu V)^2$) versus absolute value of mean signal (μV) of data pooled from (A). The variance shows linear scaling (Black line represent linear fit) with increasing NV-ODMR optical signal, indicating shot-noise limited regime in SP mode at high signal averaging of 30-ms time constant pooled together. (C)-(D) Standard deviation versus MW frequency applied (C) and Scatter plot (D) of variance versus absolute mean signal for SP Mode, low pass filter time constant 1ms. No NV-ODMR optical signal dependent scaling of noise was found, indicating Gaussian noise regime. (E)-(F) Standard deviation versus MW frequency applied (C) and Scatter plot (D) of variance versus absolute mean signal for an example responding WM pixel, acquired at 22 cycles (low) optical signal averaging. No NV-ODMR optical signal dependent scaling of noise was found, indicating Gaussian noise regime. (G)-(H) Standard deviation versus MW frequency applied (G) and Scatter plot (H) of variance versus absolute mean signal for an example responding WM pixel, acquired at 202 cycles (high) optical signal averaging. No NV-ODMR optical signal dependent scaling of noise was found, indicating Gaussian noise regime.

statistics versus applied MW frequencies at low frame averaging cycles, 22 cycles, and high frame averaging cycles, 202 cycles, for the same NV modulation frequency of 6.25 kHz to investigate the dominant noise type. At each microwave frequency, 20 widefield frames were collected to gather noise statistics. An example WM pixel, with significant NV-ODMR response, was selected from both cases (low and high averaging cycles) to represent observed noise statistics. We observed Gaussian noise dominance for both WM cases, of low averaging cycles (see Fig. 4(E)-(F)) and of high averaging cycles (see Fig. 4(G)-(H)). The baseline shift of the standard deviation (in pixel arbitrary units) with increase in averaging cycles (Fig. 4(E) and (G)), indicates camera readout noise as the main source of noise.

C. Dynamic Widefield Magnetic Imaging

Here, we describe the acquisition of millisecond widefield magnetic field images. To perform real-time imaging, the applied microwave frequency is fixed to a specific NV resonant frequency along one-axis. An externally applied magnetic field causes a linear shift in lock-in voltage (SP mode) or pixel intensity (WM mode), proportional to the zero-crossing NV slope. Therefore, tracking pixel intensities, scaled by the slope, gives a measure of the external magnetic field fluctuation along the chosen NV

axis corresponding to each pixel. The time-dependent magnetic field can be estimated from

$$B(t) = \frac{v(t) - v_o}{\left. \frac{dV_{\text{lock}}}{df} \right|_{V_{\text{lock}}=0, f=\omega_{\text{res}}}} \gamma \quad (5)$$

where $v(t)$ is the time-dependent voltage or lock-in pixel intensity, v_o is a fixed offset baseline of the pixel and $\gamma = 28 \text{ kHz}/\mu\text{T}$ is the gyromagnetic ratio. The zero-crossing slope scale factor has been independently determined corresponding to each pixel in the imaging window. Individual pixels are slightly heterogeneous in their resonant frequencies due to small deviation arising from local crystal strain and temperature effects in the excitation volume of the diamond sample. The distribution of resonant frequencies of pixels has been shown in Supplementary Figure S5A, falling within $\sim 500 \text{ kHz}$. Therefore, we chose to select the median resonant frequency from the distribution of resonant frequencies in the imaging window for widefield magnetic field tracking. A calibrated circular coil (Supplementary section 1) is used to apply a test magnetic field of known magnitude. The current in the coil is gated by a switch and controlled by a digital pulse, referred to as control pulse, see Fig. 1(a). A square wave modulated magnetic field of known frequency is applied.

Fig 5(a) shows the single-axis magnetic field tracking of a square wave field at specific time points varying

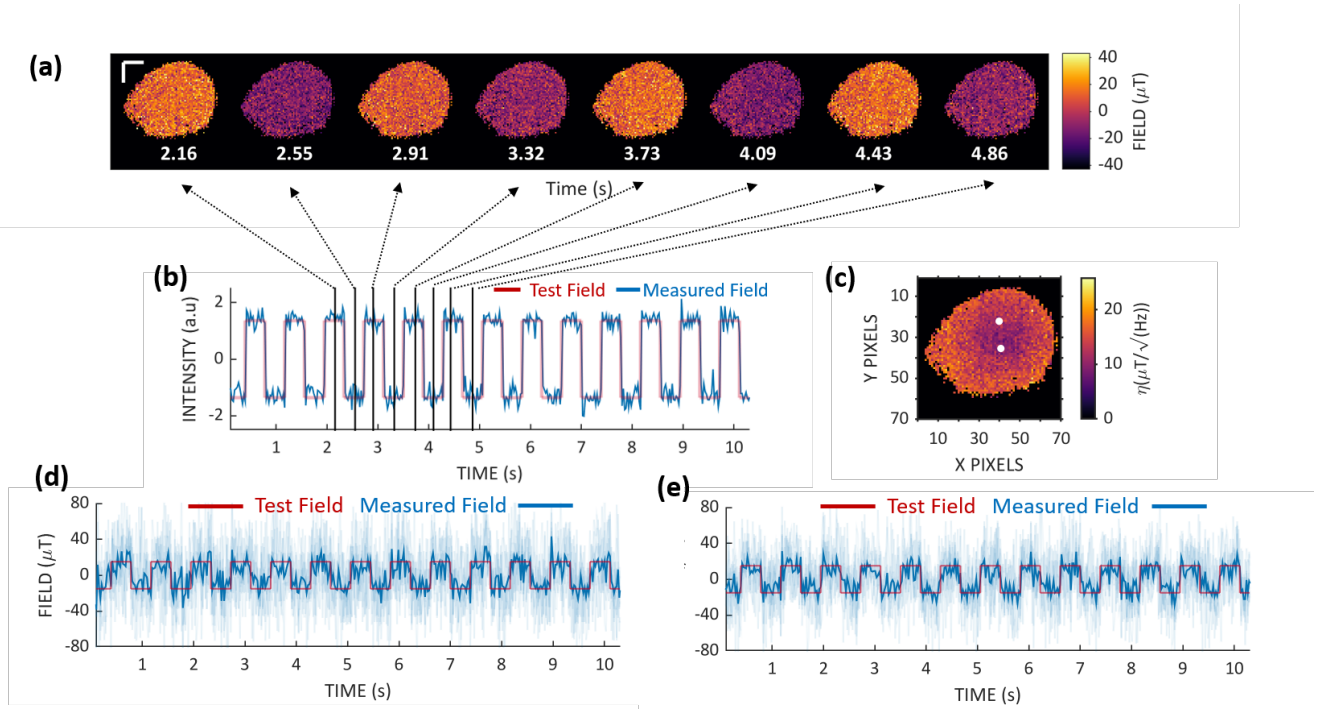


FIG. 5. Dynamic widefield magnetic field images (A) Millisecond wide-field magnetic field images, containing color-coded magnetic field response of all responding pixels, has been shown at example time instances, marked by arrows. Data color axis has been saturated to 0.7 fraction of maximum range to limit high frequency noise from masking the magnetic field response. Color map Units in $\mu\text{T}/\sqrt{\text{Hz}}$. The magnetic field images have been averaged over $N=10$ iterations. These images have been acquired at 38.6Hz frame rate and applied square wave magnetic field variation at 1.28Hz and of amplitude $30.2 \mu\text{T}$. Color map units in $\mu\text{T}/\sqrt{\text{Hz}}$ and time units labeled below images in seconds. White scale bars represent 15 pixels in the camera plane (B) Synchronization of applied square wave magnetic field with the acquisition of multiple frames in each iteration. Blue curve denotes mean pixel intensity of all responding pixels for fourth iteration. Y axis Units - arbitrary camera output baseline zeroed, X axis time in seconds. Red Curve shows the timing of applied control pulse for switching magnetic field on or off (y axis of red curve is irrelevant). Vertical black lines indicate timepoints at which widefield images response has been shown, connected with arrows (C) 2D sensitivity map of all responding pixels for this tracking dataset. Example pixels whose traces are shown ahead are marked with white dots. Colormap units are in $\mu\text{T}/\sqrt{\text{Hz}}$, X and Y Pixels denote actual pixels on the lock-in camera array, each pixel of size $40 \times 40 \mu\text{m}^2$ (D)-(E) Example single pixel intensity traces, scaled to the magnetic field values, have been shown across time. Light translucent blue curves correspond to multiple single iteration data. Dark Blue curve shows mean magnetic field trace of the pixel for $N=10$ iterations. Red curve shows applied magnetic field waveform. Spatial location of the two example pixels are marked with white dots in the sensitivity map

at 1.28 Hz. The widefield field images are acquired at 25.9 ms per frame corresponding to an imaging frame rate of 38.6 Hz and averaged over 10 iterations. Further, Fig. 5(b) shows the periodic fluctuation of mean pixel intensities in the imaging window in-sync with the applied control pulse confirming the successful tracking of an externally applied field. The test square wave magnetic field is mean subtracted and centered at zero for convenient comparison of tracking profiles with a peak-to-peak magnitude of $30.2 \mu\text{T}$. We demonstrate that the PL variation and hence, magnetic field traces of individual pixels accurately track the applied magnetic field waveform, with the corroborating time period and field amplitude at millisecond temporal resolution. The single-shot magnetic field traces and mean magnetic field traces over 10 repetitions, of two example pixels spatially marked in Fig. 5(c), have been shown in Fig. 5(d) and (e). Fig. 5(c)

also depicts the 2D per-pixel sensitivity map corresponding to the 38.6Hz frame rate data with mean and median sensitivity $13.82 \mu\text{T}/\sqrt{\text{Hz}}$ and $13.88 \mu\text{T}/\sqrt{\text{Hz}}$ respectively. (see Supplementary Note 2, point 7 for explanation on asymmetrical nature of the map). We found high frequency noise in pixel PL traces which can be reduced by the use of appropriate filtering techniques. To the best of our knowledge, the acquired single-axis wide-field magnetic field images constitute a novel demonstration of real-time millisecond scale widefield magnetometry. The fast temporal imaging demonstrated here has been enabled by increase in per-pixel SNR due to the lock-in detection scheme employed here.

Iteration-wise mean response of pixels are synchronized in phase if the pixels track the applied magnetic field in time with sufficient SNR and can serve as a simple measure to verify periodic magnetic field variations

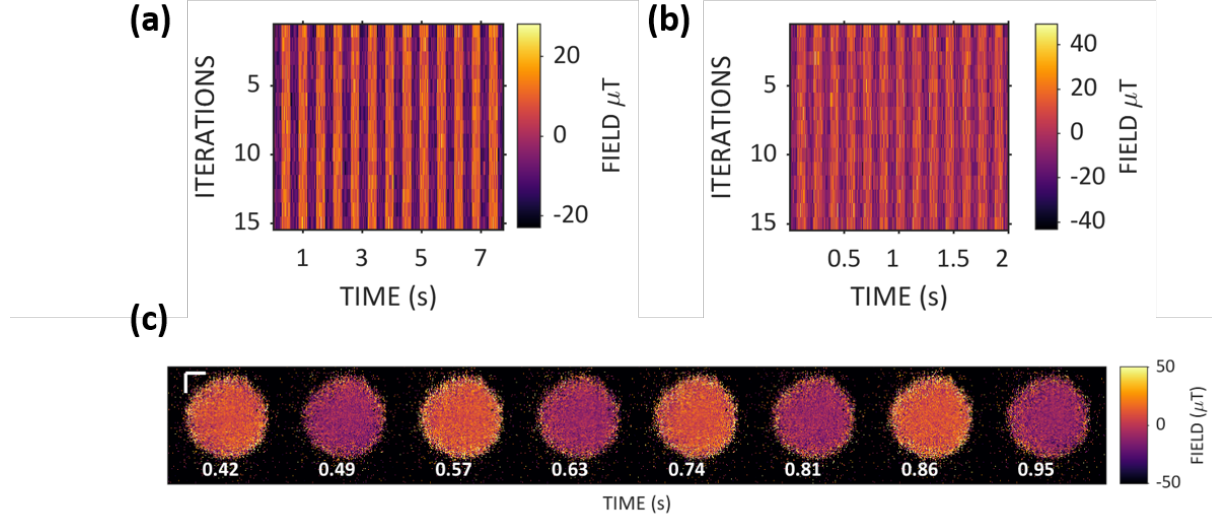


FIG. 6. Magnetic field tracking at millisecond timescales (A) Iterwise mean magnetic field response of all responding pixels for imaging frame rate 51.2 Hz, magnetic field variation 1.7 Hz, obtained from diamond NV widefield magnetometry. Aligned response profile across multiple iterations show tracking of the applied magnetic field variation. Colormap units are in $\mu\text{T}/\sqrt{\text{Hz}}$, applied field $33.37 \mu\text{T}$. (B) Iterwise mean magnetic field response of all responding pixels for imaging frame rate 198 Hz, magnetic field variation 6.61 Hz, obtained from diamond NV widefield magnetometry. Aligned response profile across multiple iterations show tracking of the applied magnetic field variation, but with lower signal-to-noise ratio. Colormap units are in $\mu\text{T}/\sqrt{\text{Hz}}$, applied field $33.37 \mu\text{T}$. (C) Dynamic wide-field magnetic field images at 198 Hz imaging frame rate, containing color-coded magnetic field response of all responding pixels, has been shown at example time instances. Data color axis has been saturated to 0.2 fraction of maximum range to limit high frequency noise from masking the magnetic field response and to saturate non-responding pixels at the edge. Color map Units in $\mu\text{T}/\sqrt{\text{Hz}}$. The magnetic field images have been averaged over $N=15$ iterations. These images have been acquired at 198Hz frame rate and applied magnetic field variation at 6.61Hz. Color map units in $\mu\text{T}/\sqrt{\text{Hz}}$ and time units labeled below images in seconds. White scale bars represent 25 pixels in the camera plane.

as shown in Fig. 6(a). The imaging frame rate can be further improved by increasing the NV modulation frequency to 8.33 kHz and decreasing the number of averaging cycles per frame. We observed clear magnetic field tracking at the cost of reduced SNR for imaging frame rate as high as 198Hz (5ms per frame), shown by synchronized iteration-wise mean response in Fig. 6(b). The magnetic field variation was 6.61Hz with an amplitude of $33.37 \mu\text{T}$. The corresponding dynamic WM images, at 198 Hz frame rate, show tracking of the applied magnetic field (Fig. 6(c)). At high imaging frame rates, the SNR is primarily limited by the NV's emitted fluorescence rate from the diamond sample, and not by the lock-in camera demodulation rates. The imaging performance demonstrated in this work is expected to improve one-two fold with the use state-of-art ion-irradiated high density Nitrogen vacancy diamond samples used in recent diamond WM magnetometry experiments.

Imaging speed and sensitivity trade-off: We discuss the interplay of four key parameters of WM imaging method, namely, the imaging frame rate I , the mean per-pixel sensitivity η , the NV modulation frequency ω_{mod} and the number of frame averaging cycles n_{cyc} . A phenomenological understanding of the coupling of parameters will be useful in deciding the trade-off. To max-

imize the imaging frame rate $I \propto \omega_{mod}/n_{cyc}$, we need to modulate NVs faster (increase ω_{mod}) and average for lesser number of frames (decrease n_{cyc}). Increasing ω_{mod} lead to a decrease in the zero-crossing NV slope but the noise σ remains mostly constant. Therefore, η will drop at higher ω_{mod} , keeping n_{cyc} same. Increasing the n_{cyc} has more interesting effects on η , since the camera read-out noise σ increases with more n_{cyc} but the NV signal strength also improves. Therefore, a multi-parameter optimization is required for understanding the trade-offs and zone of best performance for the sensor for the given specific application.

In summary, we have demonstrated significantly fast, milliseconds scale, magnetic field imaging, at 5 – 20 ms acquisition time per frame, using widefield per-pixel lock-in detection of fm-ODMR from NV centers in diamond. The widefield per-pixel lock-in method proposed here marks significant improvement from conventional ODMR imaging, where few to several minutes of averaging time is required to obtain single magnetic field images.

IV. CONCLUSION AND OUTLOOK

In this work, we have developed an experimental technique to perform real-time widefield magnetic field imaging using diamond NV centers in diamond. Per-pixel SNR is significantly enhanced using lock-in detection techniques implemented on a commercial lock-in camera which allows simultaneous demodulation of multiple pixels. While previous diamond NV based magnetometers have shown acquisition rate of several minutes per frame, we demonstrate magnetic field imaging at field variations of timescale around 1-Hz at sampling frame rate of ~ 40 Hz and also, 7 Hz at sampling frame rate of 200 Hz. The fm-ODMR protocol used in this demonstration is easy to implement, demanding only frequency modulated NV-PL and microsecond digital pulses that control camera frame demodulation. We report per-pixel sensitivity and SP bulk sensitivity much lower than recent diamond NV-widefield imaging papers [4, 11, 42, 43]. We account for these sensitivity differences to the use of non-irradiated, low NV density diamond samples in our study. Prior diamond NV implantation research [44, 45] shows that there can be up to two orders of enhancement in NV emitted red light after electron or proton irradiation with subsequent annealing. Our SP bulk sensitivity of $11.6 \text{ nT}/\sqrt{\text{Hz}}$ is ~ 1000 times lower than recent bulk diamond NV magnetometers [20, 32, 33], ranging around $15 - 50 \text{ pT}/\sqrt{\text{Hz}}$, with similar collection optics but irradiated high NV density samples. In addition to the expected improvement in magnetic field sensitivity per-pixel with extension to high NV concentration diamond samples, the spatial resolution or the temporal resolution or both in expected to improve significantly. Further, we emphasize that while we operate the camera at demodulation of $6.25 - 8.33 \text{ kHz}$ and imaging frame rates of $\sim 50 - 200 \text{ Hz}$, we are primarily limited by low NV red light from the sample and not by maximum achievable lock-in modulation rates (possible up to 250 kHz) and imaging frame rates (maximum possible 3.2 kHz) for the camera used here. Other lock-in cameras [46, 47] are expected to offer similar high frame rate advantages. During the preparation of our manuscript, we have been aware of two very recently published papers along similar lines, Hart *et al.* [43] and Kazi *et al.* [42]. Hart *et al.* employ double quantum Ramsay sequences, with the same lock-in camera, to substantially remove resonant frequency heterogeneity in different pixels. Kazi *et al.* also use a different double quantum protocol to eliminate sen-

sor inhomogeneities and demonstrate dynamic widefield microscopy examples using conventional CCD imaging. In comparison, we use the simplest form of fm-ODMR protocol, which does not need complex light and microwave pulse synchronization and is significantly easier to implement. As compared to conventional CCD imaging methods, lock-in based NV imaging allow for much faster imaging frame rates. The performance of the sensor can be further enhanced by advanced techniques taking into account the spatial inhomogeneities in the diamond sample, thereby allowing magnetic imaging of a large class of magnetic field samples.

V. AUTHOR CONTRIBUTIONS

M.P, S.B, and K.S conceived the idea. M.P and K.S designed the experimental setup. M.P constructed the experimental setup, wrote custom software for experiment control and data acquisition and performed all primary experiments and data analysis. D.S., A.B and A.G assisted data collection, fabricated and characterized microwave loop PCB and the current-switching coil assembly. D.S and S.B contributed key ideas to experiments and data analysis. M.P and K.S. wrote the manuscript in discussion with S.B. All authors reviewed and approved of the manuscript. K.S supervised all aspects of the work.

ACKNOWLEDGMENTS

K.S. acknowledges financial support from IIT Bombay seed grant number 17IRCCSG009, DST Inspire Faculty Fellowship - DST/ INSPIRE/04/2016/002284, SERB EMR grant Number EMR/2016/007420 and AOARD R&D grant No. FA2386-19-1-4042. This work was also supported by the DBT/Wellcome Trust India Alliance Fellowship IA/I/11/2500270 awarded to S.B.. M.P. thanks MHRD, India for Institute Fellowship and Prime Minister's Research Fellowship (PMRF). The authors thank Heliotis Helicam technical assistance, especially Istvan Biro, for his help in camera synchronization. K.S. acknowledges the contribution of Aditya Malusare and Parth Jatakia during the initial experimental setup. The authors thank Dr. Siddharth Tallur for lending the SR860 Lockin amplifier for SP experiments. The authors note that the work has been provisionally filed under the Indian Patent Act with application number:202121010532.

[1] S. Steinert, F. Dolde, P. Neumann, A. Aird, B. Naydenov, G. Balasubramanian, F. Jelezko, and J. Wrachtrup, *Rev. Sci. Instrum.* **81**, 043705 (2010).

[2] L. M. Pham, D. L. Sage, P. L. Stanwix, T. K. Yeung, D. Glenn, A. Trifonov, P. Cappellaro, P. R. Hemmer, M. D. Lukin, H. Park, A. Yacoby, and R. L. Walsworth, *New J. Phys.* **13**, 045021 (2011).

- [3] D. Le Sage, K. Arai, D. R. Glenn, S. J. DeVience, L. M. Pham, L. Rahn-Lee, M. D. Lukin, A. Yacoby, A. Komeili, and R. L. Walsworth, *Nature* **496**, 486 (2013).
- [4] D. R. Glenn, R. R. Fu, P. Kehayias, D. Le Sage, E. A. Lima, B. P. Weiss, and R. L. Walsworth, *Geochemistry, Geophysics, Geosystems* **18**, 3254 (2017).
- [5] E. V. Levine, M. J. Turner, P. Kehayias, C. A. Hart, N. Langellier, R. Trubko, D. R. Glenn, R. R. Fu, and R. L. Walsworth, *Nanophotonics* **8**, 1945 (2019).
- [6] J.-P. Tetienne, N. Dontschuk, D. A. Broadway, A. Stacey, D. A. Simpson, and L. C. Hollenberg, *Science advances* **3**, e1602429 (2017).
- [7] T. Wolf, P. Neumann, K. Nakamura, H. Sumiya, T. Ohshima, J. Isoya, and J. Wrachtrup, *Phys. Rev. X* **5**, 041001 (2015).
- [8] J. F. Barry, M. J. Turner, J. M. Schloss, D. R. Glenn, Y. Song, M. D. Lukin, H. Park, and R. L. Walsworth, *Proceedings of the National Academy of Sciences* **113**, 14133 (2016).
- [9] L. Rondin, J.-P. Tetienne, T. Hingant, J.-F. Roch, P. Maletinsky, and V. Jacques, *Reports on progress in physics* **77**, 056503 (2014).
- [10] G. Petrini, E. Moreva, E. Bernardi, P. Traina, G. Tomagra, V. Carabelli, I. P. Degiovanni, and M. Genovese, *Advanced Quantum Technologies* **3**, 2000066 (2020).
- [11] H. C. Davis, P. Ramesh, A. Bhatnagar, A. Lee-Gosselin, J. F. Barry, D. R. Glenn, R. L. Walsworth, and M. G. Shapiro, *Nature communications* **9**, 1 (2018).
- [12] M. J. H. Ku, T. X. Zhou, Q. Li, Y. J. Shin, J. K. Shi, C. Burch, L. E. Anderson, A. T. Pierce, Y. Xie, A. Hamo, U. Vool, H. Zhang, F. Casola, T. Taniguchi, K. Watanabe, M. M. Fogler, P. Kim, A. Yacoby, and R. L. Walsworth, *Nature* **583**, 537 (2020).
- [13] F. Casola, T. van der Sar, and A. Yacoby, *Nat. Rev. Mater* **3**, 17088 (2018).
- [14] M. J. Turner, N. Langellier, R. Bainbridge, D. Walters, S. Meesala, T. M. Babinec, P. Kehayias, A. Yacoby, E. Hu, M. Lončar, *et al.*, *Physical Review Applied* **14**, 014097 (2020).
- [15] K. Mizuno, H. Ishiwata, Y. Masuyama, T. Iwasaki, and M. Hatano, *Scientific Reports* **10**, 1 (2020).
- [16] S. E. Lillie, N. Dontschuk, D. A. Broadway, D. L. Creedon, L. C. L. Hollenberg, and J.-P. Tetienne, *Phys. Rev. Applied* **12**, 024018 (2019).
- [17] D. A. Broadway, N. Dontschuk, A. Tsai, S. E. Lillie, C. T.-K. Lew, J. C. McCallum, B. C. Johnson, M. W. Doherty, A. Stacey, L. C. L. Hollenberg, and J.-P. Tetienne, *Nature Electronics* **1**, 502 (2018).
- [18] S. E. Lillie, D. A. Broadway, N. Dontschuk, S. C. Scholten, B. C. Johnson, S. Wolf, S. Rachel, L. C. L. Hollenberg, and J.-P. Tetienne, *Nano Letters* **20**, 1855 (2020).
- [19] M. Mahmoudi, H. Hosseinkhani, M. Hosseinkhani, S. Boutry, A. Simchi, W. S. Journeay, K. Subramani, and S. Laurent, *Chemical Reviews* **111**, 253 (2011).
- [20] J. F. Barry, M. J. Turner, J. M. Schloss, D. R. Glenn, Y. Song, M. D. Lukin, H. Park, and R. L. Walsworth, *Proceedings of the National Academy of Sciences* **113**, 14133 (2016).
- [21] J. C. Price, R. Mesquita-Ribeiro, F. Dajas-Bailador, and M. L. Mather, *Frontiers in Physics* **8**, 255 (2020).
- [22] J. L. Webb, L. Troise, N. W. Hansen, C. Olsson, A. M. Wojciechowski, J. Achard, O. Brinza, R. Staacke, M. Kieschnick, J. Meijer, A. Thielscher, J.-F. Perrier, K. Berg-Sørensen, A. Huck, and U. L. Andersen, *Scientific Reports* **11**, 2412 (2021).
- [23] M. Parashar, K. Saha, and S. Bandyopadhyay, *Communications Physics* **3**, 174 (2020).
- [24] M. Schlierf, F. Berkemeier, and M. Rief, *Biophysical Journal* **93**, 3989 (2007).
- [25] V. Shah, S. Knappe, P. D. D. Schwindt, and J. Kitching, *Nature Photonics* **1**, 649 (2007).
- [26] S. Beer and P. Seitz, in *Research in Microelectronics and Electronics, 2005 PhD*, Vol. 2 (2005) pp. 135–138.
- [27] A. M. Changhui Yang and J. Alford, *Systems and methods for quasi-ballistic photon optical coherence tomography in diffusive scattering media using a lock-in camera detector*, US Patent US10881300B2 (2021).
- [28] Y. Liu, Y. Shen, C. Ma, J. Shi, and L. V. Wang, *Applied physics letters* **108**, 231106 (2016).
- [29] A. H. Meier and T. Roesgen, *Experiments in Fluids* **52**, 1017 (2012).
- [30] L. C. Sinclair, K. C. Cossel, T. Coffey, J. Ye, and E. A. Cornell, *Phys. Rev. Lett.* **107**, 093002 (2011).
- [31] R. S. Schoenfeld and W. Harneit, *Physical review letters* **106**, 030802 (2011).
- [32] J. M. Schloss, J. F. Barry, M. J. Turner, and R. L. Walsworth, *Physical Review Applied* **10**, 034044 (2018).
- [33] H. Clevenson, L. M. Pham, C. Teale, K. Johnson, D. Englund, and D. Braje, *Applied Physics Letters* **112**, 252406 (2018).
- [34] J. L. Webb, J. D. Clement, L. Troise, S. Ahmadi, G. J. Johansen, A. Huck, and U. L. Andersen, *Applied Physics Letters* **114**, 231103 (2019).
- [35] A. M. Wojciechowski, M. Karadas, A. Huck, C. Osterkamp, S. Jankuhn, J. Meijer, F. Jelezko, and U. L. Andersen, *Review of Scientific Instruments* **89**, 031501 (2018).
- [36] *Heliotis helicam™ c3 “lock-in camera*.
- [37] G. Kucsko, P. C. Maurer, N. Y. Yao, M. Kubo, H. J. Noh, P. K. Lo, H. Park, and M. D. Lukin, *Nature* **500**, 54 (2013).
- [38] M. Fujiwara, A. Dohms, K. Suto, Y. Nishimura, K. Oshimi, Y. Teki, K. Cai, O. Benson, and Y. Shikano, *Phys. Rev. Research* **2**, 043415 (2020).
- [39] M. Fujiwara, S. Sun, A. Dohms, Y. Nishimura, K. Suto, Y. Takezawa, K. Oshimi, L. Zhao, N. Sadzak, Y. Ume-hara, Y. Teki, N. Komatsu, O. Benson, Y. Shikano, and E. Kage-Nakadai, *Science Advances* **6**, 10.1126/sci-adv.aba9636 (2020).
- [40] Z. Ma, D. Zheng, Y. Fu, H. Yuan, W. Guo, J. Zhao, B. Li, Y. Shi, X. Zhang, and J. Liu, *Japanese Journal of Applied Physics* **58**, 050919 (2019).
- [41] J. M. Taylor, P. Cappellaro, L. Childress, L. Jiang, D. Budker, P. R. Hemmer, A. Yacoby, R. Walsworth, and M. D. Lukin, *Nature Physics* **4**, 810 (2008).
- [42] Z. Kazi, I. M. Shelby, H. Watanabe, Fu, K. M. C. Itoh, V. Shutthanandan, P. A. Wiggins, and KaiMei. C. Fu, *Physical Review Applied* **15**, 054032 (2021).
- [43] C. A. Hart, J. M. Schloss, M. J. Turner, P. J. Scheidegger, E. Bauch, and R. L. Walsworth, *Phys. Rev. Applied* **15**, 044020 (2021).
- [44] V. M. Acosta, E. Bauch, M. P. Ledbetter, C. Santori, K.-M. C. Fu, P. E. Barclay, R. G. Beausoleil, H. Linget, J. F. Roch, F. Treussart, S. Chemerisov, W. Gawlik, and D. Budker, *Phys. Rev. B* **80**, 115202 (2009).

- [45] A. J. Healey, A. Stacey, B. C. Johnson, D. A. Broadway, T. Teraji, D. A. Simpson, J.-P. Tetienne, and L. C. L. Hollenberg, *Phys. Rev. Materials* **4**, 104605 (2020).
- [46] H. T. Cao, D. D. Brown, P. J. Veitch, and D. J. Ottaway, *Opt. Express* **28**, 14405 (2020).
- [47] J. A. Changhui Yang, Adam Marblestone and C. Wentz, *System and method for simultaneously detecting phase modulated optical signals*, US Patents US10016137B1 (2018).

Lock-in Detection based Dynamic Widefield Magnetometry using Quantum Defects in Diamond: Supplementary Information

I. APPLIED MAGNETIC FIELD CALIBRATION

A single axis Helmholtz coil was setup near the diamond crystal. We used a two-step calibration process to deliver nanotesla range magnetic fields for SP magnetic field tracking experiments in the setup. First a large current was passed through the coil to get relatively large shifts in the NV ODMR spectrum (see Fig. S1A). The precise shifts in the resonant frequency was determined by non-linear curve fitting of the lock-in ODMR curves and subsequent, resonant frequency estimation. Using the NV gyromagnetic ratio of 28 MHz/mT, the magnitude of magnetic field measured along the NV axes was calculated. The proportionality constant was measured for a particular geometry and location of the coil by the relation $B_{measured} = KI_{measured}$. Given that the coil position and geometry are not disturbed and the current source works in a constant current mode, the proportionality constant remains the same when providing an order lower value of current to generate test magnetic field in the range of hundreds of nanotesla. Therefore, measured lower values of current were passed to deliver nanotesla magnetic fields for magnetic field measurements. To add temporal variation, like periodic time dependent field on/off, the coil current was gated by a MOSFET switch. The switching was controlled by a 7V analog output pulse generated from a buffered arbitrary analog output generator (NIDAQ PCIe-6363 National instruments card, max AO sampling rate 2MSamples/sec). For application of field lower than ~ 100 nT, the coil was directly driven by the analog output (AO) voltage waveform, generated by the NIDAQ card AO channel(see Fig. S1B).

II. PER-PIXEL RAW DATA TO MAGNETIC FIELD MAPS

Step by step procedure to measure raw-data, process and analyze time-dependent magnetic field maps.

1. Before dynamic magnetic field tracking, we acquire a widefield lock-in ODMR spectrum of a single NV resonant feature at high microwave frequency step size of 100KHz. The resonant feature is selected on the basis of high signal response and linearity at the NV zero-crossing point *i.e.* the NV resonant frequency. This selection determines the NV axis along which the magnetic field sensing will be performed.
2. The informative red light emitted from NV centers spans a limited area on the CMOS array (300x300) pixels. Further, the NV ODMR signal of different pixels differ due to Gaussian nature of optical illumination and spatial non-uniformity of the applied microwave field. Therefore, it is important to select responding pixels. First we create an average response template by taking mean of ODMR response of all pixels, responding and non-responding pixels. The template is normalized to unit norm and the unit-norm responses of all pixels are correlated to the template, via the dot product. Pixels with projection values higher than a set threshold are selected for further processing (See Fig. S3A). 2D spatial map of selected vs not-selected pixels are shown in Fig. S3B.
3. Non-linear curve fitting is performed to fit derivative of Lorentzian profiles to each selected pixel response in the previous step. The MATLAB fit function 'lsqcurvefit' is used to perform a Levenburg-Marquadt non-linear fitting for each pixel ODMR response. 16 randomly selected pixel fits have been shown in Fig. S3C.
4. We evaluated per-pixel sensitivity based on the zero-crossing NV slope obtained from the previous step for each selected pixel. Pixels selected from criteria in step 2, but located near the edge of the NV emitted beam profile, have very low or close to nil response and lead to incorrect non-linear fits with negative values of zero-crossing slope. For our experimental settings, the phase difference between reference signal and NV emitted modulated optical signal, allows the in-phase lockin ODMR signal to move from negative to positive values. Therefore, for our current settings, the per-pixel slope must be positive and we impose this criteria to further reject very low response pixels with negative zero-crossing slope fits. 2D sensitivity map obtained at this stage is shown in

Fig.S3D. The color-axis of the sensitivity map in Fig.S3D has been saturated to show distribution of relatively high sensitivity pixels in Fig.S3E.

5. We observed that the pixels near the edge of NV emitted red light profile have very low sensitivity. Only pixels with sensitivity better than a cutoff, for example $55\mu T/\sqrt{(Hz)}$ for 200Hz imaging frame rate data in the main text, were selected and further analyzed for dynamic magnetic field tracking experiments. Therefore, a further selection cutoff was imposed and pixels with sensitivity lower than the set cutoff were also removed.
6. Responding pixels remaining after step 5, were further processed to yield dynamic magnetic field maps. The scaling of raw-data PL intensity data of these responding selected pixels to magnetic field time traces was done as described in the main text.
7. *Note on asymmetrical shape of 2D NV WM sensitivity map* The threshold based selection of pixels discussed in point 2 controls the shape of the 2D sensitivity map. If threshold is set high, pixels are removed non-uniformly from the edges and it distorts the shape of the final sensitivity map from usual elliptical shape. As example of this asymmetrical map is the sensitivity map of the 38.6Hz imaging frame rate data set in Main text , Figure 5(c) where high threshold 0.5 was applied. The 198Hz imaging frame rate presented in main text, Figure 6 (C) has symmetrical shape due to low threshold 0.05 applied.

III. SUPPLEMENTARY FIGURES

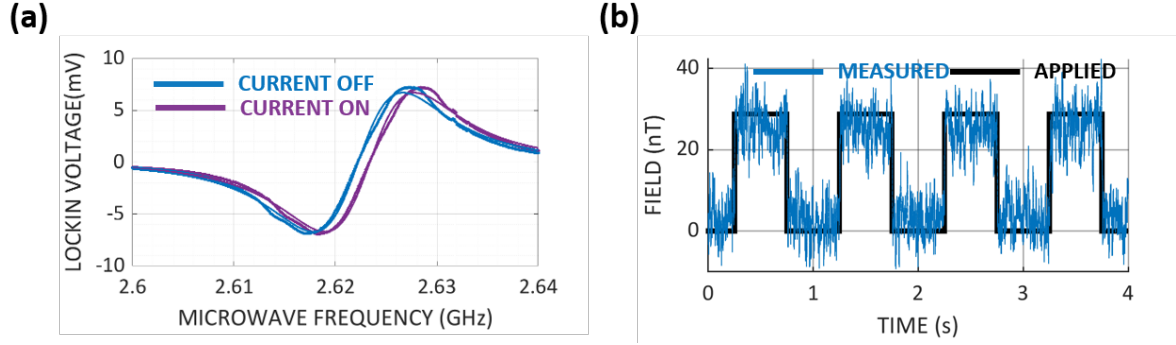


FIG. S1. Single-axis coil magnetic field calibration and single-point (SP) NV based magnetic field tracking. (A) The NV optically detected magnetic resonance (ODMR) spectrum curve shifts when a known constant current is passed through a single-axis coil. Dots represent data-points and lines represent non-linear fits of a derivative-Lorentzian curve. The proportionality constant, for a given coil location and geometry, between the magnetic field along the NV axis and the applied current is calculated from differences in current on versus off resonant frequencies and the known NV gyromagnetic ratio. (B) Real-time lock-in SP magnetometry based tracking of applied test square wave magnetic field. Blue curve represents magnetic field traces obtained from SP NV magnetometry. Black curve represents the applied test magnetic field along the particular NV axes being used for tracking. Applied field magnitude is 28.5 nT , traces have been averaged over 1000 iterations.

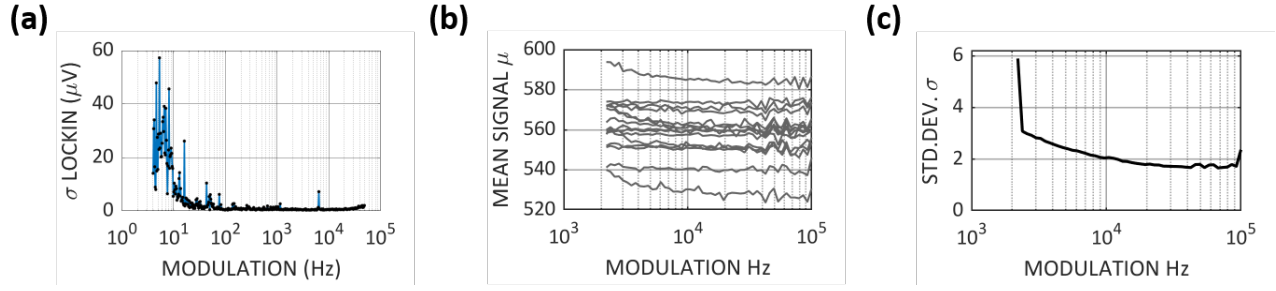


FIG. S2. Experimental noise spectrum of Single-Point (SP) and Widefield imaging (WM) magnetometry setups. (A) Noise spectrum of SP magnetometry setup across different diamond NV modulation frequency (which is same as lock-in amplifier reference). This spectrum has been measured with all experimental conditions identical to ODMR experiments except applied microwave excitation was off. Low-pass filter time constant set to 100 ms during the measurement. (B) Mean Noise measured for randomly chosen 15 pixels of the lock-in camera measured across different modulation frequencies. Similar to part A, experimental conditions were same as widefield ODMR experiments except microwave excitation was off. Units reflect 1024 (10-bit) points scale of camera output (C) Mean curve of standard deviation of randomly chosen 10000 pixels of the lockin camera versus diamond NV modulation frequencies. Part B and Part C data obtained from same set of data of camera lockin intensity frames ($n=20$) at different modulation frequencies ($n=20$ frames collected at each modulation frequency). Units reflected 1024 (10-bit) points scale of camera output. We note that the minimum camera lockin frequency is 2.2KHz , and therefore high noise at lower frequencies are not observed, unlike part A SP measurements.

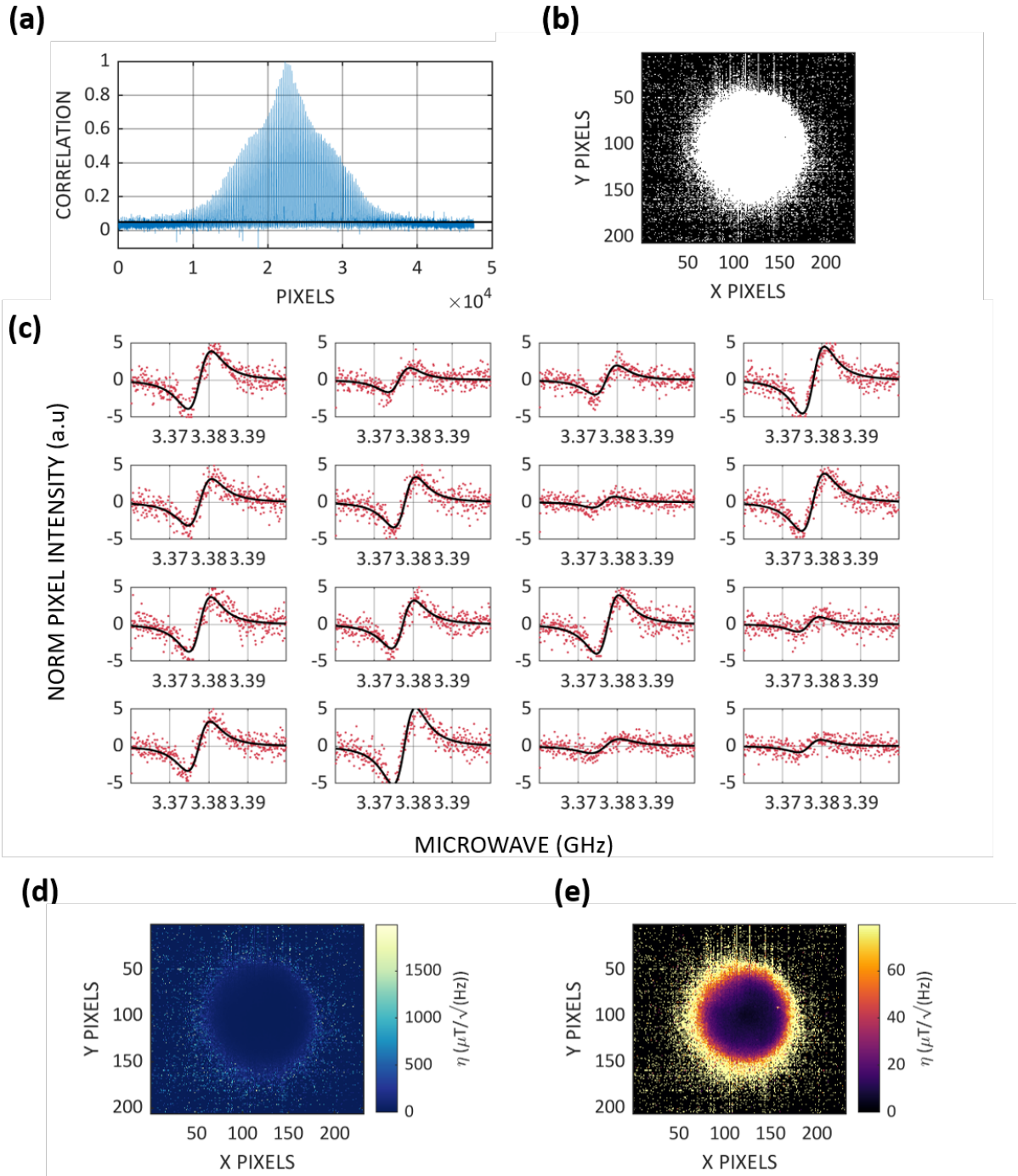


FIG. S3. Selection of pixels with high NV- optically detected magnetic resonance (ODMR) response from diamond NV widefield imaging data. (A) Projection values of the normalized NV-ODMR response of all pixels on a mean NV-ODMR template for selection of pixels with relatively high peak-to-peak NV-ODMR signal. Heterogeneity in per-pixel response arises from heterogeneity in optical/microwave excitation of NV centers. Horizontal line denotes the applied threshold, 0.05, for selection of responding pixels. X axis represents number of pixels concatenated into 1D array from 2D image data. Y axis represents the values of projections of each pixel, named correlation here. (B) 2D selection mask generates from threshold selection. White represents responding pixels and black represents rejected pixels. The selection mask shape also approximately resembles the shape of optical excitation. (C) 16 example plots of non-linear curve fits on the NV-ODMR data of 16 randomly chosen pixels out of all responding pixels. A derivative of Lorentzian function was fit to each responding pixel in the 2D widefield NV-ODMR dataset. Black colored lines denote obtained curve fits and red dots denote per-pixel data. X-axis of all 16 plots represent applied microwave frequencies in GHz. Y-axis of all 16 plots represent baseline zeroed pixel intensities in arbitrary units of camera digital output (D) 2D Sensitivity map obtained, after further rejection of pixels with negative slope fits. Due to relatively small number of very-low sensitivity pixels at the periphery of the profile, the distribution of high-sensitivity pixels is not visible in this map (E) 2D pixel sensitivity map, same as in part D but with color axis saturated to 0.04 fraction to show the spatial distribution of high sensitivity pixels.

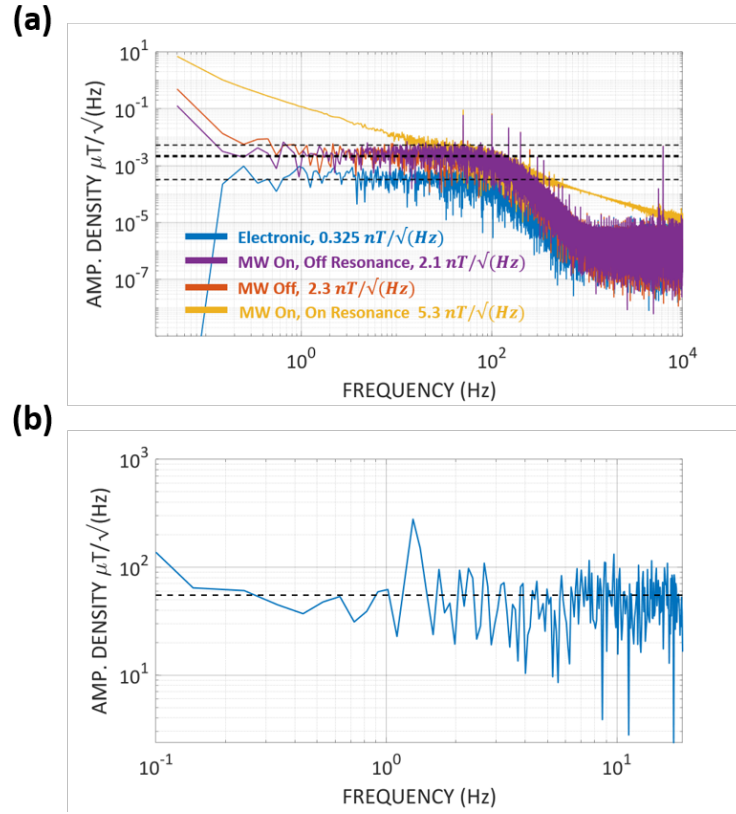


FIG. S4. Fourier magnetic noise density of single-point magnetometry (SP) and widefield magnetometry (WM) (A) Amplitude spectral density (ASD) of magnetic field tracking noise for SP magnetometry for four different cases - electronic noise, microwave (MW) on with off resonance MW frequency applied, MW on with on resonance frequency applied and MW off. Noise floor, represented by horizontal lines, have been marked by averaging ASD over 0.9Hz to 100Hz window. Mean Noise floor of $0.325, 2.1, 5.3, 2.3 \text{ nT}/\sqrt{Hz}$ were observed for the four cases respectively. Y axis units are in $\mu T/\sqrt{Hz}$ X axis units are in frequency Hz (B) Amplitude spectral density (ASD) of magnetic field tracking noise for an example pixel from widefield magnetometry, measured while tracking $30.2 \mu T$ magnetic field. Noise floor of $51.47 \mu T/\sqrt{Hz}$ has been marked by averaging ASD over 0.9Hz to 10Hz window. Y axis units are in $\mu T/\sqrt{Hz}$ X axis units are in frequency Hz .

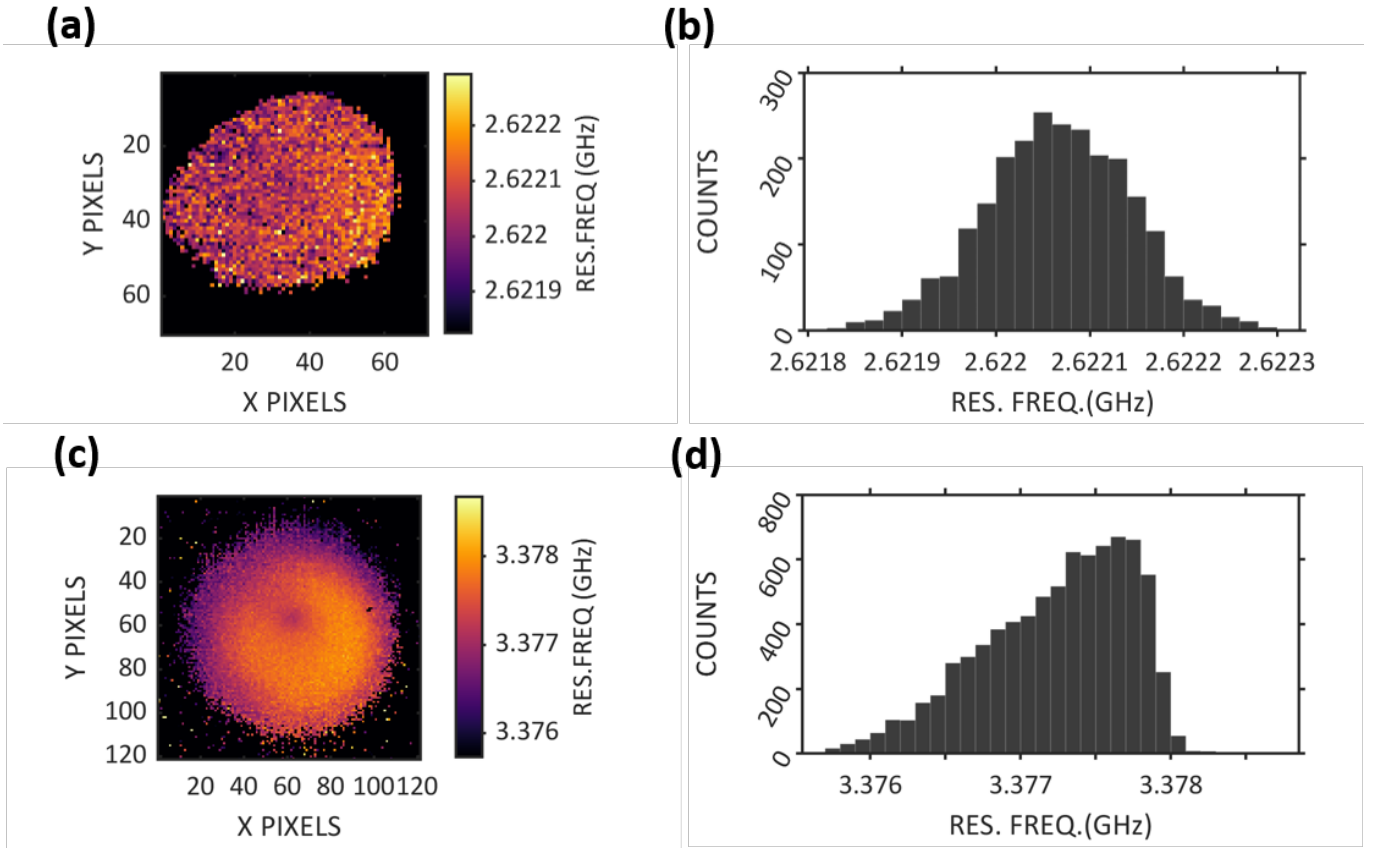


FIG. S5. Heterogeneity in resonant frequencies of different pixels. (A) 2D Spatial map of resonant frequencies of different pixels have been shown. These 2D maps are from the 38.6Hz imaging frame rate dataset, shown in the main text (B) Histogram of resonant frequencies of all pixels corresponding to the 2D map shown in part A, most pixels fall within a $\sim 500\text{KHz}$ range of variability in the resonant frequencies. (C) 2D Spatial map of resonant frequencies of different pixels have been shown. These 2D maps are from the 198Hz imaging frame rate dataset, shown in the main text (D) Histogram of resonant frequencies of all pixels corresponding to the 2D map shown in part A, most pixels fall within an $\sim 2\text{MHz}$ range of variability in the resonant frequencies.